Journal of Metals, Materials and Minerals, 36(2), e2564, 2026

Cold sintering-assisted low temperature fabrication of dense $Ba_5Nb_4O_{15}$ ceramics

Usa SUKKHA[1,2], Apichayaporn TEANDAM[2,3], Phakkhananan PAKAWANIT[4], Phitsamai KAMONPHA[5], Wanwilai VITTAYAKORN[2,6], Phieraya PULPHOL[2,3,*] and Naratip VITTAYAKORN [2,7]

[1] *Department of General Science and Liberal Arts, King Mongkut's Institute of Technology Ladkrabang, Prince of Chumphon Campus, Chumphon, 86160, Thailand*
[2] *Advanced Materials Research Unit, School of Science, King Mongkut's Institute of Technology Ladkrabang, Bangkok, 10520, Thailand*
[3] *Department of Materials Science, Faculty of Science, Srinakharinwirot University, Bangkok, 10110, Thailand*
[4] *Synchrotron Light Research Institute, Nakhon Ratchasima, 30000, Thailand*
[5] *National Institute of Reference Laboratories, Department of Science Service, Ministry of Higher Education, Science, Research and Innovation, Bangkok, 10400, Thailand*
[6] *Department of Nanoscience and Nanotechnology, School of Integrated Innovative Technology, King Mongkut's Institute of Technology Ladkrabang, Bangkok, 10520, Thailand*
[7] *Department of Chemistry, School of Science, King Mongkut's Institute of Technology Ladkrabang, Bangkok, 10520, Thailand*

***Corresponding author e-mail**: phieraya@g.swu.ac.th

Received date:
13 November 2025
Revised date:
19 January 2026
Accepted date:
10 February 2026

Keywords:
$Ba_5Nb_4O_{15}$ ceramic;
Cold sintering process;
Transient liquid phase;
Low-temperature densification

Abstract

This study presents a novel approach for fabricating $Ba_5Nb_4O_{15}$ (BNO) ceramics at low sintering temperatures via the cold sintering process (CSP), using $Ba(OH)_2{\cdot}8H_2O$ (BOH) as a transient liquid phase. CSP was performed under an external pressure of 10 MPa with a sintering temperature range of 150°C to 300°C. Optimally, BNO-BOH ceramics achieved a relative density of 93.7 ± 0.43% when sintered at 250°C for 1 h. Scanning electron microscopy (SEM) suggested that particle densification occurred via a dissolution-precipitation process, which filled pores and formed necks between particles. The study demonstrates that the residual liquid content is crucial for ceramic densification. Annealing the as-cold sintered BNO-BOH ceramics at 1000°C for 1 h successfully eliminates the $BaCO_3$ secondary phase. Furthermore, dielectric properties of annealed ceramics were also characterized at room temperature from frequency range of 20 Hz to 2 MHz. The dielectric permittivity is reported to be 39.2 and 0.01 for tan δ at 1.8 MHz. The cold sintering process provides an effective strategy to reduce the sintering temperature while achieving high relative density. This method offers a promising alternative for the fabrication of advanced ceramics.

1. Introduction

The wireless communications market is experiencing rapid expansion. This growth is driven by surging demand and the ongoing evolution of the ecosystem from 5G toward 6G [1,2]. As networks progress toward 6G, they will utilize wider channel bandwidths at millimeter-wave (mm-Wave) and sub-terahertz (sub-THz) frequencies. This advancement necessitates denser multi-antenna front ends and imposes tighter requirements on materials regarding both loss and thermal stability. Consequently, this development has created a growing need for various specialized components within these systems, such as antennas, filters, and resonators [3,4]. These components require specific properties. Firstly, a suitable relative dielectric permittivity ($10 < \varepsilon_r < 100$) is essential. Secondly, they must exhibit low dielectric loss, defined by a high quality factor ($Q \times f > 50$ THz). Finally, a near zero temperature coefficient of resonant frequency ($\tau_f \approx 0$ ppm·°C^{-1}) is crucial [5,6].

$Ba_5Nb_4O_{15}$ (BNO) holds particular importance as a benchmark lead-free microwave dielectric. It shows a moderate relative permittivity ($\varepsilon_r \approx 40$), a high quality factor ($Q \times f \approx 27{,}200$ GHz), and a positive temperature coefficient of resonant frequency ($\tau_f \approx +78$ ppm·°C^{-1}) [7-10]. Typically, dense BNO ceramics require firing at 1200°C to 1500°C for 2 h to 6 h to develop the microstructure necessary for low loss and stable dielectric properties [7-9]. However, such high firing temperatures present several challenges. They increase energy consumption and cost, promote Ba volatilization and cation non-stoichiometry, and can trigger the formation of secondary phases that degrades $Q \times f$ and shifts the resonant frequency. To overcome these issues and decrease the sintering temperature, glassy sintering aids (e.g., $BaWO_4$, ZnB_2O_5, B_2O_3-SiO_2) have been introduced into BNO. This approach can reduce the sintering temperature by 500°C to 600°C relative to conventional firing [10-12]. Nevertheless, the residual intergranular glass can act as impurities. These impurities subsequently increase dielectric loss and perturb τ_f, resulting in lower $Q \times f$ value [10-12].

Over the past decade, the cold sintering process (CSP) has emerged as a significant method for densifying ceramics. This technique, pioneered by C. Randall *et al.*, achieves densification at ultra-low temperatures (<400°C) by combining a transient liquid phase (TLP)

with externally applied pressure [13-16]. Key factors influencing densification include temperature, applied pressure, time, and the TLP. Optimal densification also relies on carefully controlled process parameters. For instance, applied pressure (ranging from tens to hundreds of MPa) enhances particle contact and drives dissolution [17-19]. While, excessive pressure can disrupt the crucial liquid films. Similarly, temperature (from room temperature to 400°C) is a critical factor for accelerating kinetics. However, insufficient temperatures will hinder dissolution process. On the other hand, temperatures that are too high lead to the premature evaporation of the liquid, which halts densification. Sufficient dwelling time is necessary for the solubility of the host ceramic and the evaporation of transient liquid phase. This evaporation leads to the supersaturation stage [20]. However, an excess of transient liquid can slow this process, as precipitation only occurs after that liquid has evaporated [18,21]. Furthermore, any residual liquid may leave pores upon evaporation, which subsequently lowers the relative density [19]. Insufficient liquid phase inhibits mass transport and results in incomplete densification. This is because the TLP serves as both solvent and a rapid transport medium. It enables stress-assisted dissolution-precipitation, which is the primary mass transport mechanism for ceramics. Therefore, an appropriate amount of TLP content (typically 1wt% to 20 wt%) is essential. This range ensures the formation of continuous liquid films, thereby enabling effective stress-enhanced dissolution, diffusion, and reprecipitation [13,14].

The CSP has been successfully applied to numerous microwave-relevant dielectrics. Demonstrations have achieved over 90% relative density in systems such as Li_2MoO_4-Al_2O_3, $Zn_3B_2O_6$, CaF_2, BaF_2, and Na_2WO_4 [22-27]. This success underscores CPS's potential for developing energy-efficient, Ag-cofireable components. Nevertheless, most successful CSP demonstrations have been limited to systems involving soluble oxides or acid solutions. In contrast, the exploration of hydrates containing structural water as a TLP has been notably rare. One exception is $BaTiO_3$, which has been cold sintered with $Ba(OH)_2{\cdot}8H_2O$ to achieve relative densities up to ~97% [28,29]. In this specific case, the hydrate flux provides the TLP that accelerates surface transport and neck growth. Recently, our previous work used $Ba(OH)_2{\cdot}8H_2O$ (BOH) as a transient liquid phase to prepare $Ba_5Nb_4O_{15}$ (BNO) ceramics by cold sintering process. The mixed powders were pre-heated at 80°C for 30 min to release H_2O molecules from BOH. Then, the temperature was elevated to the desired sintering temperatures. From these process, the ceramics only achieved ~80% relative density [30]. This limited densification may be attributed to inappropriate or unoptimized cold sintering conditions, indicating a need for process redesign. Furthermore, our results showed a drastic change in relative density as applied pressure increases. However, only a slight change in relative density occurs when the applied pressure increased from 7 MPa to 10 MPa. This suggests that other factors beyond pressure need adjustment to obtain high density ceramics. In this work we specifically focus on the effect of residual TLP on the densification process. It is important to consider that a pre-heating step at 80°C for 30 min may lead to water loss. Such loss could result in an insufficient amount for the subsequent densification process. Moreover, prior research indicates that pre-heating time significantly influences densification by affecting the amount of water available during the dissolution-precipitation process. A direct consequence of insufficient water content is a reduction in ceramic density, as reported by J. Hao *et al.* [27].

To optimize the cold sintering of BNO, we adopted two key modifications. Firstly, we eliminate the pre-heating step. Simultaneously, we adjusted the BNO:BOH ratio. Furthermore, we investigated the influence of sintering temperature on densification process. This single-step process offers significant advantages. It demonstratable enhances densification, prevents undesirable reactions, and maintains a low co-firing temperature. These benefits provide a practical and efficient route to produce dense BNO.

2. Materials and methods

2.1 Powder preparation

$Ba_5Nb_4O_{15}$ powder was synthesized using the solid-state reaction method as depicted in Figure 1(a). Reagent grade powders of $BaCO_3$ (98.5 % purity, Sigma) and Nb_2O_5 (99.9% purity, Inframat) were stoichiometrically weighed according to $Ba_5Nb_4O_{15}$ formula and mixed using horizontal ball mill technique in ethanol and zirconia ball for 18 h. The slurry was then dried in a hot air oven at 80°C overnight. The mixed powder was calcined at 1200°C for 6 h with a heating rate of $5°C{\cdot}min^{-1}$. After that, the calcined powders were ground and sieved to obtain fine powder for the surface treatment.

2.2 Surface treatment for $Ba_5Nb_4O_{15}$ powder

To facilitate dissolution-precipitation and densification during cold sintering, an amorphous layer was created on the surface of the BNO powder. Following the procedure in Figure 1(b), 10 g of BNO powder was treated with 50 mL of 1 $mol{\cdot}L^{-1}$ acetic acid solution at 80°C for 1 h. Then, the treated powder was filtered, washed with deionized water to a pH of 7, and dried overnight at 80°C in a hot air oven. This surface-treated BNO, referred to as ST-BNO, was used for preparation of BNO ceramics.

2.3 Cold sintering process (CSP)

Firstly, we investigated whether the pre-heating step (80°C for 30 min) employed in previous work [30] caused excessive evaporation of water, which acts as the TLP. ST-BNO powder was thoroughly mixed with barium hydroxide octahydrate ($Ba(OH)_2{\cdot}8H_2O$ or BOH, 98.5 purity, Qrec) at an established 5:1 weight ratio (ST-BNO: BOH). Crucially, these samples were then cold sintered at 150°C to 300°C under a uniaxial pressure of 10 MPa for 1 h without the pre-heating step. It was found that all ceramics processed without pre-heating retained a high residual water content, which was not observed in the previous work. Furthermore, the density of these samples was not significantly different from that of a green body. This finding confirms that, in the absence of the pre-heating step, the amount of TLP (water) was excessively high, thereby hindering proper densification. Consequently, this experiment also confirms that water loss occurs during both the pre-heating step and the CSP itself. Based on this insight, we subsequently adjusted the ST-BNO:BOH ratio to 10:1. This modification aimed to reduce the initial water content and thereby improve the final ceramic densification.

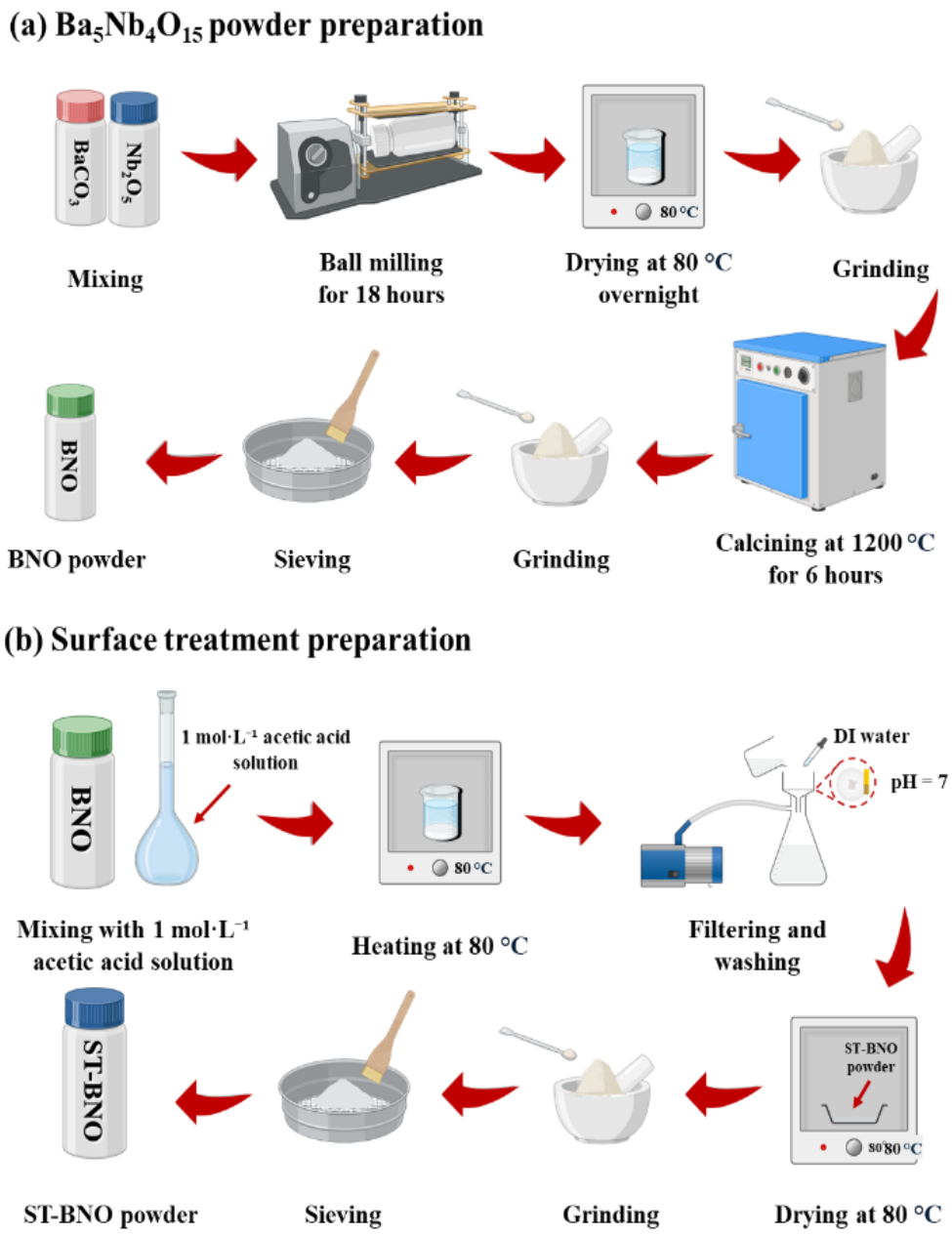

Figure 1. Illustrative overview of (a) $Ba_5Nb_4O_{15}$ powder preparation, and (b) $Ba_5Nb_4O_{15}$ powder surface treatment.

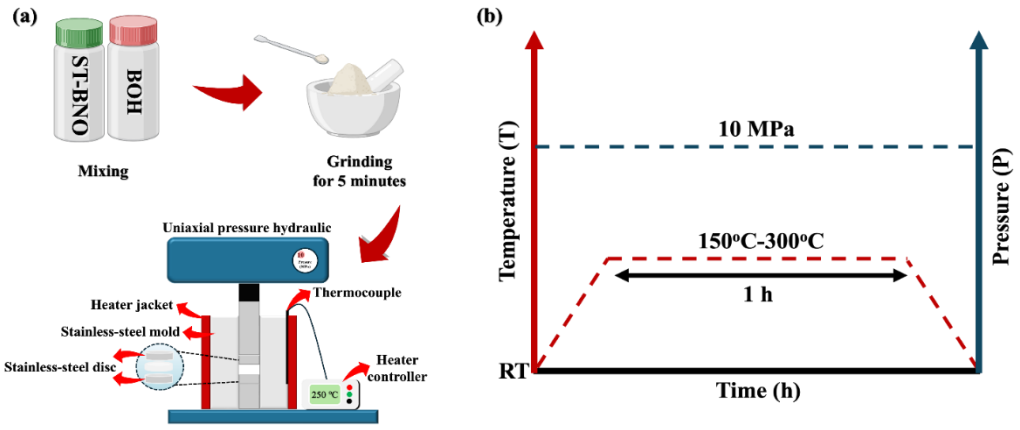

Figure 2. Schematic illustration of the cold sintering process for BNO-BOH ceramics, showing (a) the preparation steps, and (b) the cold-sintering conditions.

The optimized condition for this study involves using 0.6 g of ST-BNO and 0.06 g of BOH. These powders were mixed using a mortar and pestle for 5 min. The mixed powder was then loaded into a stainless-steel mold with a diameter of 10 mm. The mold was covered with a heater jacket as shown in Figure 2(a). A constant uniaxial pressure of 10 MPa was initially applied to the die at room temperature. Without a pre-heating step, the temperature was then raised to the desired sintering temperature at a rate of 10°C·min^{-1} and held for 1 h. In addition, the effect of sintering temperature on the relative density of BNO-BOH ceramic was investigated between 150°C and 300°C, as shown in Figure 2(b). The as-cold sintered BNO-BOH ceramics that show the highest density were selected to further anneal at 800°C to 1000°C for 1 h with a heating rate of 5°C·min^{-1}.

2.4 Characterization

To determine the density of the ceramic pellets, the Archimedes method was employed using a balance-density kit (Model ML-T 43, Mettler Toledo, LLC, USA). The relative density of the sample pellets was calculated from the Equation (1) [31].

$$\rho_{\text{rel}} = \left(\frac{\rho_{\text{exp}}}{\rho_{\text{th}}}\right) \times 100\% \quad (1)$$

where ρ_{rel} is the relative density (%), ρ_{exp} is the experimental density, and ρ_{th} is the theoretical density. The functional groups of BNO ceramics were characterized using Attenuated Total Reflectance-Fourier Transform Infrared spectroscopy (ATR-FTIR, ALPHA II, Bruker, Switzerland). The ATR-FTIR spectra were recorded in the wavenumber range of 550 cm^{-1} to 1600 cm^{-1}. Phase formation and purity of the BNO and ST-BNO powders and BNO-BOH ceramics were investigated using an X-ray diffractometer (XRD, Empyrean, Cu K_α radiation, PANalytical, Netherlands). XRD data were collected in the 2θ scan range of 20° to 80° at a step size of 0.01°. For crystallographic information of BNO and ST-BNO powders, XRD data were analyzed using Le Bail refinement from JANA2006 software. Prior to XRD and ATR-FTIR measurements, BNO-BOH ceramics were ground into fine powder. The microstructure and elemental composition of the BNO-BOH ceramics was studied using a field emission scanning electron microscope (FE-SEM, Thermo Scientific, Apreo S, USA) equipped with an energy dispersive X-ray spectrometer (EDS, Oxford, XMax). To prevent charge buildup on the sample surface, BNO-BOH samples were sputter-coated with a gold layer before characterization. Furthermore, the true 3-dimensional internal structures of ceramic with the highest density were studied using synchrotron radiation X-ray tomography (SR-XTM) at beamline 1.2 W, SLRI, Thailand. X-ray projections of samples were collected in the angular range of 0° to 180° with 0.1 angular increment. Sample projections were collected on a sCMOS camera with a pixel size of 1.44 μm. The data were reconstructed using Octopus Reconstruction software, and a 3D visualization of the volume was then generated with Drishti software. Additionally, the dielectric properties were studied using LCR meter (Agilent, E4980A, USA). The sample surfaces were coated with conductive silver paint to create conductive electrical contacts. Measurements were taken over a frequency range of 20 Hz to 2 MHz at room temperature.

3. Results and discussion

The XRD technique was employed to analyze the phase formation and purity of both BNO and ST-BNO powders. To confirm phase purity and obtain detailed structural information, the XRD analysis was performed by Le Bail refinement method using the JANA2020 software. The XRD were refined with trigonal symmetry (space group P-3m1), based on standard crystallographic information from the Crystallography Open Database (COD). Typical Le Bail refinement plots, illustrating the fit between the experimental and calculated diffraction patterns, are presented in Figure 3(a-b). It is clearly seen that the refined XRD profiles of BNO and ST-BNO powders correspond well with the experimental XRD profile across the entire measured 2θ range. Furthermore, the refinement parameters and quality of fit are summarized in Table 1. The experimental XRD data for both the BNO powder and the ST-BNO powder showed good agreement with theoretical standards. Specifically, the corresponding R_{wp} and GOF values are 11.00% and 1.88 for BNO, and 11.33% and 1.93 for ST-BNO. These results confirm that both the BNO and ST-BNO powders possess a pure $Ba_5Nb_4O_{15}$ phase with trigonal symmetry. This indicates that the surface treatment with a 1 mol·L^{-1} acetic acid solution neither generated any secondary crystalline phases nor altered the crystal structure of the ST-BNO powders.

The ATR-FTIR spectra of BNO and ST-BNO powders are presented in Figure 3(d). For the BNO powder, characteristic absorption bands are observed within the wavenumber range of 500 cm^{-1} to 1000 cm^{-1}, consistent with reports in the literatures [32,33]. Specifically, absorption bands appear at 658 cm^{-1} and 750 cm^{-1} which are assigned to stretching vibration of Nb-O-Nb and Nb-O, respectively. As expected, the IR spectrum of the ST-BNO powder also exhibits two absorption bands within this same range. This observation is consistent with the XRD results, which show that the acetic acid treatment neither affected the crystal structure or generated secondary phases in the ST-BNO powder.

Table 1. Refinement parameters of BNO powder and ST-BNO powder obtained from Le Bail refinement.

Parameter	Sample	
	BNO	**ST-BNO**
R_p (%)	7.41	7.58
R_{wp} (%)	11.00	11.33
GOF (%)	1.88	1.93
a (Å)	5.79329(7)	5.79364(7)
b (Å)	5.79329(7)	5.79364(7)
c (Å)	11.7874(2)	11.7867(2)
Space group	*P-3m1*	
Structure	Trigonal	

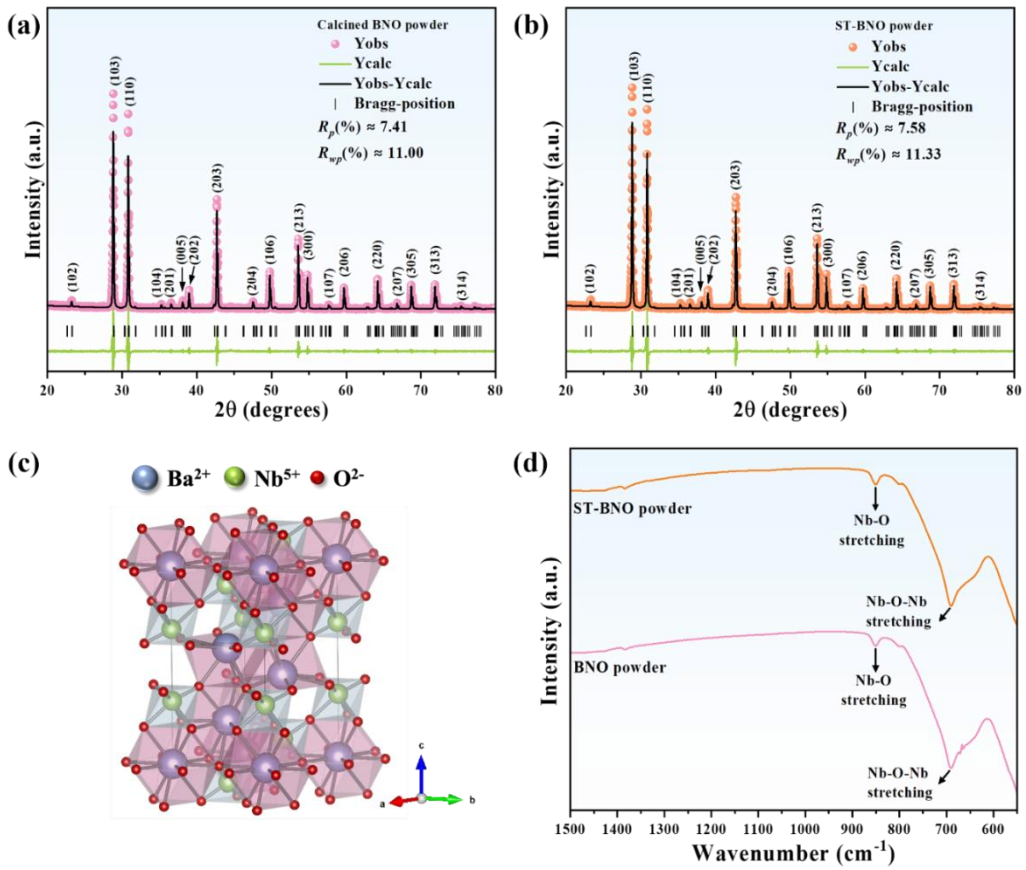

Figure 3. XRD patterns of (a) BNO powder calcined at 1200°C for 6 h, (b) ST-BNO powder, (c) crystal structure of BNO, and (d) ATR-FTIR spectra of BNO powder and ST-BNO powder.

Figure 4(a-e) presents SEM images illustrating the microstructures of the BNO-BOH green body and BNO-BOH ceramics cold sintered at 10 MPa for 1 h across the 150°C to 300°C temperature range. Insets in these figures include digital photographs of these samples, which all appear as white pellets with approximately 1 cm in diameter and 1 mm in thickness. The green body pressed at 25°C showed particle compaction with non-uniform morphology (Figure 4(a)). The particle size of the compacted green body is in the range between 0.201 µm to 6.349 µm. The surface also exhibited micro-sized pores distributed throughout, measuring around 0.04 µm to 1.466 µm. The relative density of the green body is 64.8 ± 0.89%. Cold sintered BNO-BOH ceramic at 150°C shows an uneven surface and visible pores (Figure 4(b)). Compared to the green body, particle size significantly decreases to approximately 0.122 µm to 2.703 µm, with pore size of 0.108 µm to 1.738 µm. Furthermore, few neck formation areas are observed in some parts of the ceramic surface as marked by the circle in Figure 4(b). These results suggest the initiation of the dissolution-precipitation mechanism at 150°C. As the temperature is elevated to 200°C, both particle and pore sizes continue to decrease significantly to 0.108 µm to 2.506 µm and 0.02 µm to 1.401 µm, respectively. Neck formation becomes noticeably more pronounced at this temperature, confirming enhanced mass transport. At 250°C, the ceramic shows a smooth surface with only a few small pores. Thus, it could be said that across the temperature range of 150°C to 250°C, the particle size, pore size and total porosity systematically decrease as the cold sintering temperature increases. However, when the sintering temperature is raised to 300°C, a change in microstructure occurs as the neck formation decreases. The pore size becomes larger (0.02 µm to 0.572 µm) compared to that of the ceramic sintered at 250°C. Furthermore, the ceramic sintered at 250°C for 1 h with external pressure of 10 MPa which shows the optimum condition was selected for SR-XTM imaging to study the internal microstructure. Figure 4(f) illustrates the SR-XTM image with rather dense ceramic corresponding to the surface microstructure results from SEM. The theoretical, experimental, and calculated relative densities of the cold-sintered BNO-BOH ceramics are presented in Figure 4(g). The sample sintered at 150°C achieves a relative density of 89.8 ± 0.74%, which represents a significant improvement from the relative density of the green body (64.8 ± 0.89%). With increasing sintering temperature to 200°C and 250°C, the relative density increased to 92.2 ± 0.34% and 93.7 ± 0.43%, respectively. This result indicates the enhancement of densification. However, when the temperature reached 300°C, the relative density declined to 90 ± 0.24% . The relative density results are related to the microstructure characterization from SEM. Furthermore, the elemental composition of the powders and ceramics was determined via EDX analysis, as summarized in Table 2. The results for all samples reveal a Ba:Nb:O atomic ratio aligning closely with the expected $Ba_5Nb_4O_{15}$ stoichiometry.

The densification mechanism of cold sintered BNO-BOH in this work can be proposed across various stages. At the initial stage of cold sintering, the main densification mechanism is dominated by mechanical forces while the BOH remains in its solid form, crystalline state $Ba(OH)_2{\cdot}8H_2O$. Applied external pressure drives the initial

rearrangement and compaction of the dry BNO and solid BOH powders (see Figure 5(a)). Some particle sliding occurs even in solid state due to mechanical force and fracture of particles. Then, it can help reduce large voids and increase the contact area. When the temperature reaches the sintering range (150°C to 300°C), which is above the melting point of $Ba(OH)_2{\cdot}8H_2O$ [28], H_2O molecules are released. This released water acts as a lubricant, accelerating particle motion and initiating the dissolution of BNO particles. Under continuous external pressure, the transient liquid phase facilitates extensive and efficient particle sliding, which is crucial for achieving high packing density before neck formation begins.

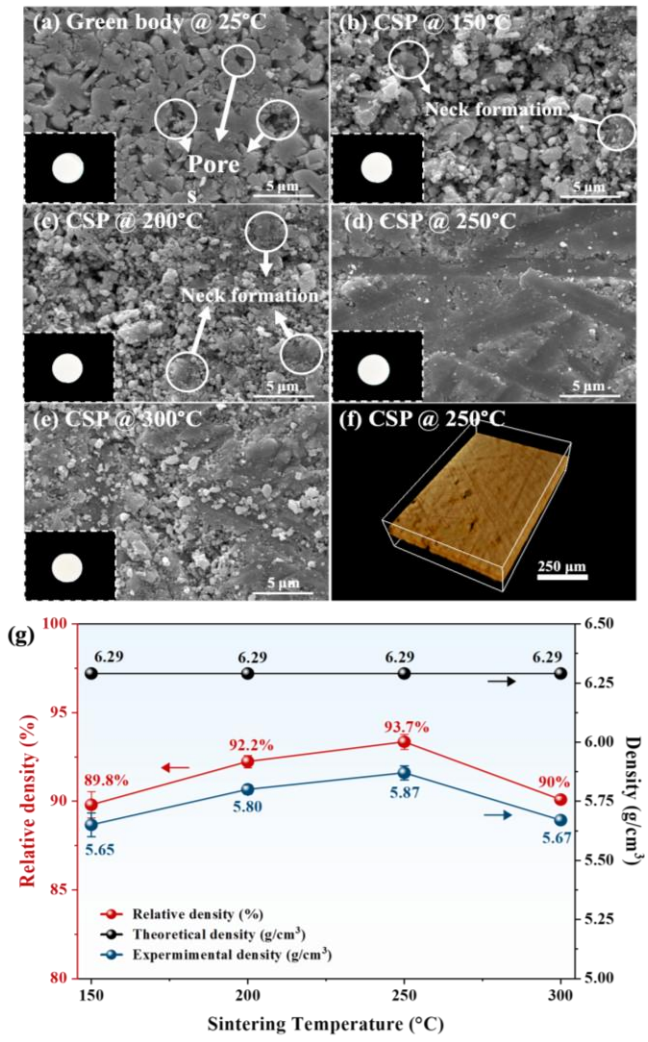

Figure 4. SEM images of (a) the BNO-BOH green body, and cold sintered BNO-BOH ceramics at 10 MPa for 1 h at (b) 150°C, (c) 200°C, (d) 250°C, (e) 300°C, (f) the SR-XTM image of the cold sintered BNO-BOH at 250°C, and (g) densities of cold sintered BNO-BOH ceramics as a function of sintering temperature.

The dissolution of soluble species from BNO particles into the transient liquid phase coincides with the dissociation of $Ba(OH)_2{\cdot}xH_2O$ into Ba^{2+} ions. Drawing an analogy from the cold sintering of other Ba-based ceramics provides insight into the multifaceted role of these ions. In the well-studied case of acid-treated $BaTiO_3$ reported by H. Guo *et al.* and A. Ndayishimiye *et al*., their work involved treating the $BaTiO_3$ surface with acid prior to CSP, which resulted in surface leaching via incongruent dissolution. It was found that the dissolution rate of Ba^{2+} ions exceeded that of Ti^{4+}, leading to the formation of a Ti-rich amorphous layer on the particle surfaces [14,34]. Furthermore, T. Sada *et al.* studied the preparation of $BaTiO_3$ ceramics via a cold sintering process (CSP) using acid-treated $BaTiO_3$ and $Ba(OH)_2{\cdot}8H_2O$ as the transient liquid phase. They reported that during CSP with a Ba-containing system, two distinct but complementary roles of the supplied Ba^{2+} ions were identified. The Ba^{2+} ions from the $Ba(OH)_2{\cdot}8H_2O$ TLP compensate for the stoichiometry of the final materials [35]. Additionally, T. Sada *et al.* reported that the TLP creates a chemical environment conducive to both dissolution and precipitation: it serves as a highly basic medium that promotes Ti^{4+} dissolution while simultaneously providing the high Ba^{2+} concentration necessary for $BaTiO_3$ recrystallization within pore spaces. These mechanisms are critical for neck formation and subsequent densification [28]. However, a concurrent and undesirable side effect is the reaction of Ba^{2+} ions with atmospheric CO_2, which results in the formation of $BaCO_3$ phase [28,29].

We propose that a similar mechanism governs the densification of our BNO system. The dissolved ions (from both the BNO surface and the BOH additive) are transported rapidly through the continuous aqueous film (Figure 5(b-i)). Temperature enhances both solubility and the evaporation rate, promoting the formation of a supersaturated solution. This supersaturation then drives precipitation into the pore spaces, leading to neck formation between particles (Figure 5(b-ii)). Within this general CSP framework, the dissolved Ba^{2+} ions are expected to fulfill specific functions: they (i) compensate for Ba-deficient in the amorphous surface layer of the acid-treated BNO particles, and (ii) react with dissolved Nb species to recrystallize the BNO phase at interparticle necks, thereby directly driving densification. Simultaneously, a portion of the $Ba(OH)_2$ may react with ambient CO_2 during the process, resulting in the formation of a $BaCO_3$ secondary phase within the ceramic (Figure 5(b-iii)) [28]. The detection of $BaCO_3$ in our as-cold sintered samples by XRD confirms this side reaction, aligning with the previous work [28,29]. This comprehensive framework explains how Ba^{2+} ions contribute positively to densification while also accounting for the transient secondary phase, which is subsequently removed via annealing.

Table 2. The results of EDX analysis with weight and atomic percentage of powders and ceramics of $Ba_5Nb_4O_{15}$.

Sample	Weight [%]			Atomic [%]		
	Ba	Nb	O	Ba	Nb	O
BNO powder	53.2	23.1	23.8	18.24	11.71	70.05
ST-BNO powder	48.4	23.9	27.7	15.05	10.99	73.96
BNO-BOH ceramic (150°C)	52.2	26.7	21.0	19.20	14.51	66.29
BNO-BOH ceramic (200°C)	54.6	29.9	16.2	23.06	18.23	58.72
BNO-BOH ceramic (250°C)	55.6	28.5	16.0	23.65	17.92	58.43
BNO-BOH ceramic (300°C)	53.6	29.3	17.1	22.00	17.77	60.23

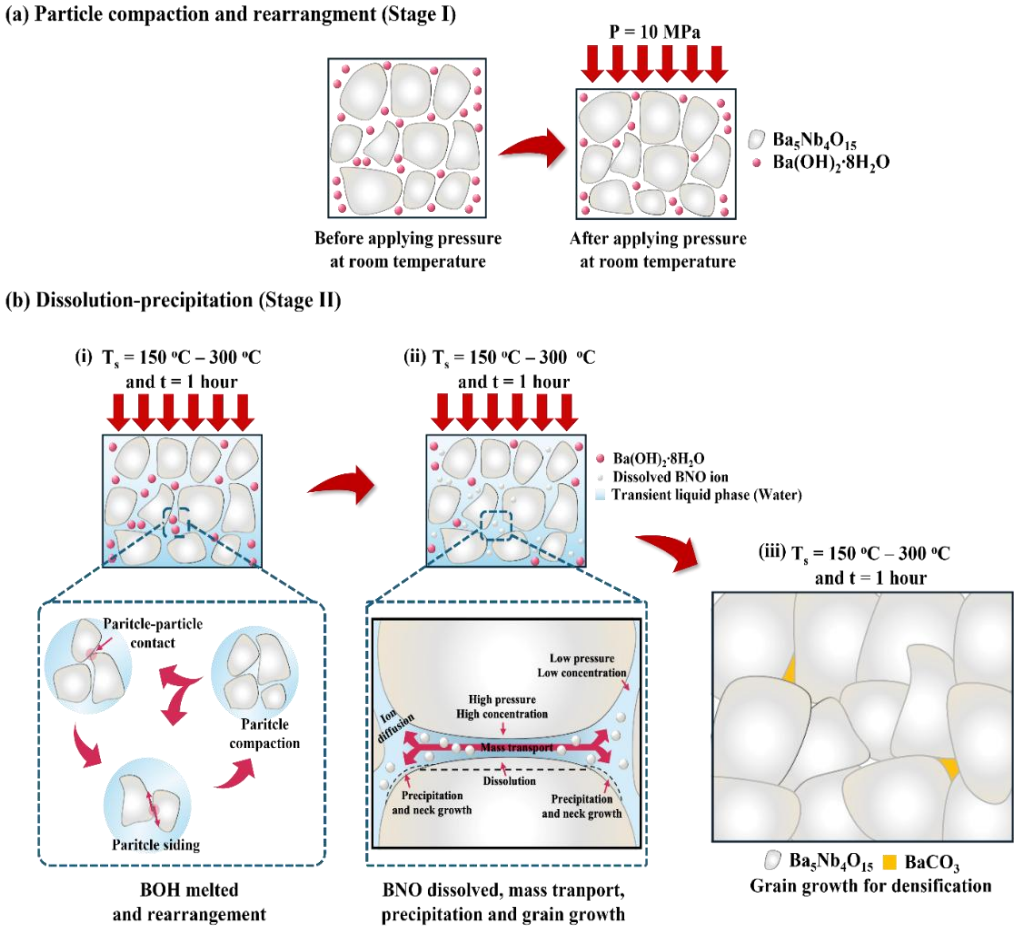

Figure 5. Proposed mechanism of the cold sintering process using $Ba(OH)_2{\cdot}8H_2O$ as a transient liquid phase, Adapted with modifications from Refs. [15, 22] (a) Stage I: External pressure facilitates particle compaction, (b) Stage II: Particle dissolved and rearrangement involving particle contact and particle sliding with dissolution-precipitation mechanism contributing to neck growth and pore filling.

The observed drop in relative density for the BNO-BOH ceramic cold sintered at 300°C is possibly due to the transient liquid phase evaporated too rapidly. When the evaporation rate exceeds the rate required for sintering, the liquid films break apart. This discontinuity weakens the capillary forces needed for rearrangement and hinders the mass transport mechanism (dissolution-diffusion-precipitation). The result is incomplete neck formation between particles and high residual porosity.

As reported in our previous study, the two-step cold sintering process, involving a pre-heating step (80°C for 30 min) and a subsequent sintering step, yielded a ceramic with a relative density of only around 80%. Since an insufficient liquid phase inhibits densification by impeding the dissolution-precipitation mass transport mechanism, we hypothesized that this low density was caused by excessive solvent evaporation during pre-heating. This is strongly supported by our current experiment: when eliminating the pre-heating step with BNO:BOH ratio of 5:1, the post-sintered sample was noticeably moist. Consequently, this finding highlights the necessity of precisely controlling the liquid phase content, as excessive water loss during pre-heating directly impedes the densification process.

Figure 6 shows the XRD patterns for the cold sintered BNO-BOH ceramics from 150°C to 300°C. All samples reveal two distinct sets of diffraction peaks, indicating the presence of two phases. As expected, the major phase is identified as barium niobate ($Ba_5Nb_4O_{15}$) (JCPDS #14-0028). A secondary minor phase is identified as barium carbonate ($BaCO_3$) (JCPDS #71-2394), indicated by a peak at $2\theta \approx 23.9$ (marked with a solid down-pointing triangle in Figure 6(a-b)). The formation of $BaCO_3$ phase as a byproduct during cold sintering is a well-documented phenomenon [28]. Our observation of $BaCO_3$ phase is consistent with the previous research by T. Sada *et al.* on cold-sintered $BaTiO_3$ that utilized $Ba(OH)_2{\cdot}8H_2O$ as a hydrate flux [28]. This $BaCO_3$ phase is formed by the reaction between $Ba(OH)_2{\cdot}xH_2O$ and CO_2 in the ambient environment, as illustrated by Equation (2) [28].

$$Ba(OH)_2{\cdot}\,xH_2O + CO_2 \rightarrow BaCO_3 + H_2O\uparrow \qquad (2)$$

Moreover, ATR-FTIR spectroscopy was utilized to confirm the presence of the $BaCO_3$ phase coexisting with BNO phase in the cold sintered ceramics. Figure 6(c) shows the ATR-FTIR spectra of the cold sintered BNO-BOH ceramics at various sintering temperatures. All samples show three absorption bands at 658 cm^{-1}, 750 cm^{-1} and 1460 cm^{-1}. The absorption bands around 658 cm^{-1} and 750 cm^{-1} corresponded to Nb-O-Nb stretching vibration and Nb-O stretching vibration of BNO phase. The band at 1460 cm^{-1} was assigned the CO_3^{-2} asymmetric vibration which related to the functional group of carbonate [36]. This result corresponds with the XRD data, confirming that $BaCO_3$ formed during the cold sintering process.

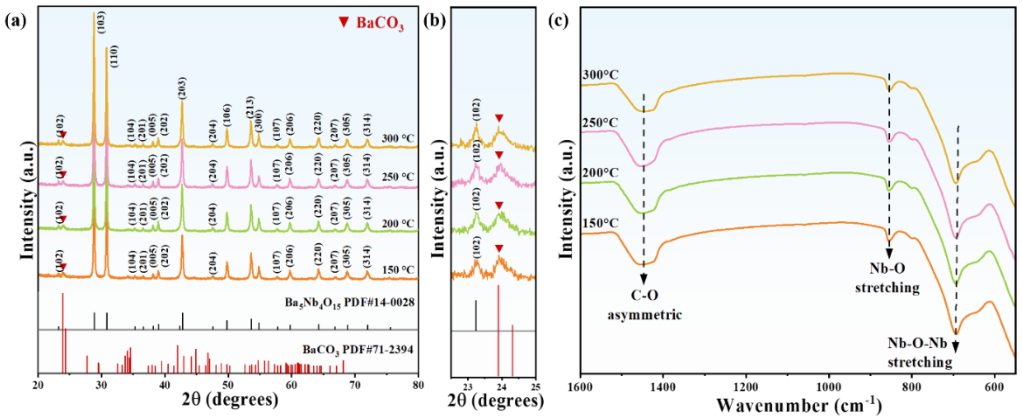

Figure 6. (a) XRD patterns of cold sintered BNO-BOH ceramics, (b) an expanded view of the XRD patterns from 2θ = 22.5° to 25°, and (c) ATR-FTIR spectra.

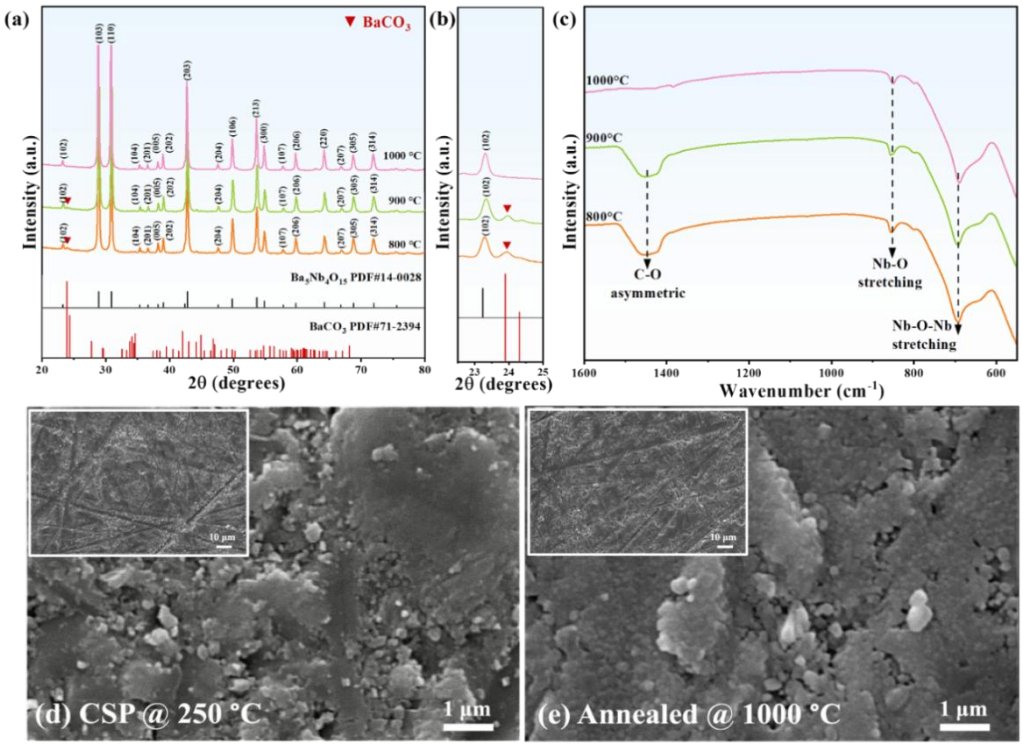

Figure 7. (a) XRD patterns of annealed BNO-BOH ceramics at various temperatures, (b) enlarged XRD patterns at (102) plane, (c) ATR-FTIR spectra of annealed BNO-BOH ceramics at various temperatures, and SEM images comparing, (d) as-cold sintered, and (e) annealed BNO-BOH ceramic at 1000°C.

The formation of a secondary phase significantly degrades the microwave dielectric properties of ceramics. Studies have shown that these phases inherently possess high dielectric loss, acting as defects that reduce the overall quality factor (Q × f) [37,38]. Furthermore, secondary phases inhibit crystalline growth, which in turn reduces the crystallinity and introduces pores. These defects elevate the dielectric loss, resulting in a decreased Q × f. The presence of these impurity phases also negatively impacts the thermal stability of the material by increasing the magnitude of the temperature coefficient of resonant frequency (τ_f) [39,40]. Therefore, to mitigate these extrinsic factors, heat treatment is necessary to eliminate the $BaCO_3$ secondary phase. Previous reports indicate that the $BaCO_3$ can be eliminated by annealing at temperature around 800°C to 1000°C [41-43]. Therefore, the as-cold sintered BNO-BOH ceramic (sintered at 250°C with maximum relative density) was selected for an annealing study to evaluate the effectiveness of this $BaCO_3$ elimination process. The annealing process was carried out at 800°C, 900°C and 1000°C for 1 h.

Figure 7(a) shows the XRD patterns of cold sintered BNO-BOH ceramics annealed at various temperatures. It is found that the $BaCO_3$ phase is still observed in the XRD patterns after annealing at 800°C and 900°C. However, the $BaCO_3$ phase is completely removed when the annealing temperature reaches 1000°C (Figure 7(a-b)). The ATR-FTIR spectra of cold sintered BNO-BOH ceramics after annealing were displayed in Figure 7(c). As expected, the absorption band at 1460 cm^{-1}, which assigned to be asymmetric vibration of the CO_3^{-2}, disappeared after annealing at 1000°C. This confirms that $BaCO_3$ can be successfully removed from cold sintered BNO-BOH ceramics by annealing at 1000°C. Furthermore, it was found that the annealing did not affect the relative density and microstructure of the cold sintered BNO-BOH ceramics. Scanning electron microscopy (SEM) confirms

that the microstructure and pore size remains identical to the as-cold sintered BNO-BOH ceramic. This suggests that the energy supplied during annealing was insufficient to promote either densification or grain growth.

As reported, BNO ceramics prepared using conventional sintering require pre-heating at 1000°C for 2.5 h then subsequent sintered at 1250°C for 2.5 h to achieve a maximum relative density of 92% [44]. In this study, densification was achieved at 93.7 ± 0.43% after cold sintered at 250°C under a uniaxial pressure of 10 MPa for 1 h, with an assistant of BOH as a flux to facilitate the dissolution-precipitation during cold sintering process. Although, the ceramics require post-annealing step at 1000°C for 1 h to eliminate the impurity $BaCO_3$ phase. This approach enables the fabrication of highly dense BNO ceramics within a significantly shorter processing time and at a much lower sintering temperature than conventional sintering methods thereby reducing energy consumption and offering a sustainable alternative route for ceramic fabrication.

Figure 8 presents the frequency-dependent dielectric properties of the annealed BNO-BOH ceramic at room temperature. At low frequencies (e.g., 20 Hz), the relative permittivity (ε_r) of the annealed BNO-BOH ceramic exhibits a remarkably high value of approximately 569. This elevated permittivity in the low-frequency regime is characteristic of materials exhibiting significant space charge polarization (also known as interfacial polarization or Maxwell-Wagner polarization) [44,45]. This phenomenon is generally observed when charge carriers accumulate at internal interfaces (e.g., grain boundaries, impurity phases, or defects) under an applied electric field, leading to a substantial increase in apparent permittivity in the low-frequency regime. As the frequency increases, the dielectric permittivity rapidly decreases due to the slower polarization mechanisms. This behavior prominently originates from the frozen space charge and some dipolar types as frequency is elevated. Their contribution to total polarization diminishes, causing the observed drop in ε_r. At approximately 1.8 MHz, the ε_r value of annealed BNO-BOH ceramic remains stable. This indicates that only the faster polarization mechanisms, primarily electronic polarization and ionic polarization, continue to respond to the alternating field.

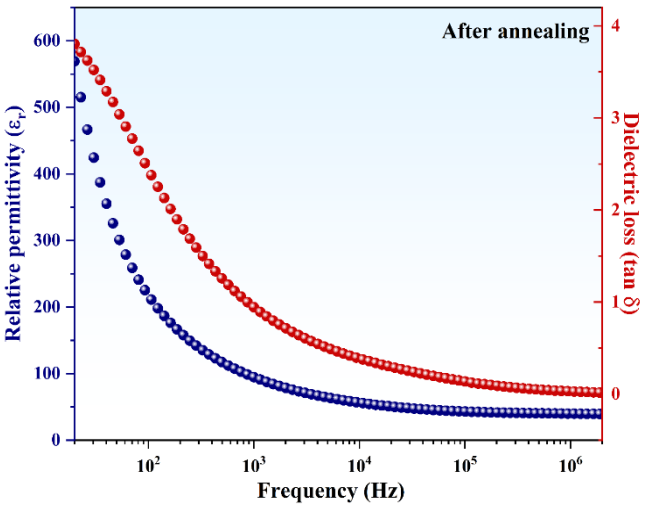

Figure 8. Dielectric properties of annealed BNO-BOH ceramic measured at room temperature with frequency range of 20 Hz to 2 MHz.

Indeed, this stable ε_r value of annealed ceramics near 39 MHz at 1.8 MHz is consistent with reported values for similar BNO-based ceramics (e.g., around 42). This strongly suggests that the combined cold sintering and annealing process effectively yields desirable bulk dielectric properties that would persist at microwave frequencies where interfacial effects are less prominent [46,47].

In addition, the dielectric loss (tan δ) tends to decrease with increasing frequency. This phenomenon can be attributed to the dipoles are unable to follow the rapidly alternating electric field, which leads to a reduction in energy dissipation [11]. While the tan δ at 1.8 MHz decreased significantly and stabilized at approximately 0.01, this value still represents a relatively high value. For typical microwave dielectric ceramic applications, a much lower tan δ (often in the range of 10 to 3 to 10 to 5, corresponding to $Q \times f$ of 1,000 to 10,000 at GHz frequencies) is required to minimize energy dissipation. The presently observed tan δ at 1.8 MHz, therefore, suggests that further optimization of the microstructure and reduction of extrinsic loss factors are critical for this cold sintered BNO-BOH ceramic to achieve performance competitive with conventionally sintered microwave dielectrics [48,49].

4. Conclusion

This study successfully demonstrates the fabrication of $Ba_5Nb_4O_{15}$ (BNO) ceramics at remarkably low temperatures using the cold sintering process (CSP). A key to this achievement is the effective utilization of $Ba(OH)_2 \cdot 8H_2O$ as a transient liquid phase (TLP). Crucially, careful adjustment of the TLP's residual amount proves essential for optimizing densification. The optimized cold sintering condition (250°C, 1 h, 10 MPa) yields BNO ceramics with a high relative density of 93.7%. This represents a 14% increase in density directly attributable to precise control over the influence of transient liquid phase. Comprehensive characterization further confirms the structural integrity, phase purity, and dense microstructure of these BNO ceramics. They also demonstrate promising dielectric performance with ε_r of 39 and low tan δ across the frequency range of 20 Hz to 2 MHz. These findings affirm CSP as a viable low-temperature route for fabricating BNO ceramics. The profound impact of managing the residual transient liquid phase, allowing for such significant improvements in density, distinctly underscores its immense potential for low-temperature processing of complex oxides and other functional materials.

Acknowledgements

This research was supported by a grant from the Graduate School's Revenue Budget, Srinakharinwirot University, for the fiscal year 2025 (Grant No. 488/2568). We also acknowledge the facilities and technical assistance from Advanced Technology Testing and Analysis Center (ATTAC) of School of Integrated Innovation Technology (SIITec), King Mongkut's Institute of Technology Ladkrabang (KMITL).

References

[1] P. Li, J. Fan, and J. Wu, "Exploring the key technologies and applications of 6G wireless communication network," *iScience,* vol. 28, no. 5, p. 112281, 2025.

[2] Z. Pi, and F. Khan, "An introduction to millimeter-wave mobile broadband systems," *IEEE Communications Magazine,* vol. 49, no. 6, pp. 101–107, 2011.

[3] Y. Zhang, J. Y. Deng, M. J. Li, D. Sun, and L. X. Guo, "A MIMO dielectric resonator antenna with improved isolation for 5G mm-wave applications," *IEEE Antennas and Wireless Propagation Letters,* vol. 18, no. 4, pp. 747–751, 2019.

[4] F.-F. Wu, D. Zhou, C. Du, B.-B. Jin, C. Li, Z.-M. Qi, S. Sun, T. Zhou, Q. Li, and X.-Q. Zhang, "Design of a sub-6 GHz dielectric resonator antenna with novel temperature-stabilized $(Sm_{1-x}Bi_x)NbO_4$ (x = 0–0.15) microwave dielectric ceramics," *ACS Applied Materials & Interfaces,* vol. 14, no. 5, pp. 7030–7038, 2022.

[5] R. Lowndes, F. Azough, R. Cernik, and R. Freer, "Structures and microwave dielectric properties of $Ca_{(1-x)}Nd_{2x/3}TiO_3$ ceramics," *Journal of the European Ceramic Society,* vol. 32, no. 14, pp. 3791–3799, 2012.

[6] H. Ohsato, "Microwave dielectrics with perovskite-type structure," in *Perovskite Materials - Synthesis, Characterisation, Properties, and Applications*, L. Pan and G. Zhu Eds. London: IntechOpen, 2016.

[7] I. N. Jawahar, P. Mohanan, and M. T. Sebastian, "$A_5B_4O_{15}$ (A=Ba, Sr, Mg, Ca, Zn; B=Nb, Ta) microwave dielectric ceramics," *Materials Letters,* vol. 57, no. 24, pp. 4043–4048, 2003.

[8] C. Vineis, P. K. Davies, T. Negas, and S. Bell, "Microwave dielectric properties of hexagonal perovskites," *Materials Research Bulletin,* vol. 31, no. 5, pp. 431–437, 1996.

[9] R. Ratheesh, M. T. Sebastian, P. Mohanan, M. E. Tobar, J. Hartnett, R. Woode, and D. G. Blair, "Microwave characterisation of $BaCe_2Ti_5O_{15}$ and $Ba_5Nb_4O_{15}$ ceramic dielectric resonators using whispering gallery mode method," *Materials Letters,* vol. 45, no. 5, pp. 279–285, 2000.

[10] H. Zhuang, Z. Yue, F. Zhao, J. Pei, and L. Li, "Microstructure and microwave dielectric properties of $Ba_5Nb_4O_{15}$–$BaWO_4$ composite ceramics," *Journal of Alloys and Compounds,* vol. 472, no. 1, pp. 411–415, 2009.

[11] J.-R. Kim, D.-W. Kim, H. S. Jung, and K. S. Hong, "Low-temperature sintering and microwave dielectric properties of $Ba_5Nb_4O_15$ with ZnB_2O_4 glass," *Journal of the European Ceramic Society,* vol. 26, no. 10, pp. 2105–2109, 2006.

[12] X. Zhou, C. Sun, D. Xia, L. Cao, Z. Wen, S. Zhang, and B. Tang, "Low-temperature sintering kinetics and dielectric properties of $Ba_5Nb_4O_{15}$ with B_2O_3–SiO_2 glass," *Journal of Materials Science: Materials in Electronics,* vol. 32, no. 7, pp. 8716–8724, 2021.

[13] C. Vakifahmetoglu, and L. Karacasulu, "Cold sintering of ceramics and glasses: A review," *Current Opinion in Solid State and Materials Science,* vol. 24, no. 1, p. 100807, 2020.

[14] A. Ndayishimiye, M. Y. Sengul, T. Sada, S. Dursun, S. H. Bang, Z. A. Grady, K. Tsuji, S. Funahashi, A. C. T. V. Duin, and C. A. Randall, "Roadmap for densification in cold sintering: Chemical pathways," *Open Ceramics,* vol. 2, p. 100019, 2020.

[15] T. Yu, J. Cheng, L. Li, B. Sun, X. Bao, and H. Zhang, "Current understanding and applications of the cold sintering process," *Frontiers of Chemical Science and Engineering,* vol. 13, no. 4, pp. 654–664, 2019.

[16] J. Guo, R. Floyd, S. Lowum, J.-P. Maria, T. H. de. Beauvoir, J.-H. Seo, and C. A. Randall, "Cold sintering: Progress, challenges, and future opportunities," *Annual Review of Materials Research,* vol. 49, pp. 275–295, 2019.

[17] J. Ding, J. Guo, R. Yan, W. Li, S. Ma, Y. Fu, W. Xie, R. Riedel, and A. Weidenkaffa, "Cold sintering process: A green route to fabricate thermoelectrics," *Journal of Advanced Ceramics,* vol. 13, no. 11, pp. 1697–1712, 2024.

[18] Y. Liu, Q. Sun, D. Wang, K. Adair, J. Liang, and X. Sun, "Development of the cold sintering process and its application in solid-state lithium batteries," *Journal of Power Sources,* vol. 393, pp. 193–203, 2018.

[19] H. Cui, C. Li, R. Muhammad, Y. Wang, Z. Qian, and K. Song, "Cold sintering and magneto-dielectric properties of (1-x) $Ni_{0.5}Zn_{0.5}Fe_2O_4$-xK_2MoO_4 composite ceramics," *Materials Research Bulletin,* vol. 179, p. 112961, 2024.

[20] H. Palneedi, P. Sharief, S.-M. Hong, J.-W. Kim, M. Uzair, S.-C. Jeon, and J. Guo, "Densification and grain growth in ceramics fabricated by cold sintering: A review on the effect of process parameters," *Journal of the American Ceramic Society,* vol. 109, no. 1, p. e70268, 2025.

[21] J. Radhakrishnan, S. Subramani, and J. L. Ocaña, "Cold sintering behaviors of barium titanates: Recent progress and impact on microstructure, densification and dielectric-ferroelectric response," *Coordination Chemistry Reviews,* vol. 502, p. 215621, 2024.

[22] D. Wang, L. Li, J. Jiang, Z. Lu, G. Wang, K. Song, D. Zhou, and I. M. Reaney, "Cold sintering of microwave dielectric ceramics and devices," *Journal of Materials Research,* vol. 36, no. 2, pp. 333–349, 2021.

[23] N. Chen, J. Cheng, X. Xu, H. Wang, X. Li, Z. Zeng, B. Zhao, M. Xu, and H. Wang, "Structure, thermal and microwave dielectric properties of cold-sintered $Li_2MoO_4Al_2O_3$ ceramic," *Journal of Materiomics,* vol. 11, no. 4, p. 100940, 2025.

[24] C. Li, Y. Liu, M. Chi, X. Luo, B. Liu, M. Mao, H. B. Bafrooei, G. Wang, E. Taheri-Nassaj, and K. Song, "ULTCC post-annealing cold sintering densification process, microwave dielectric properties of $Zn_3B_2O_6$ ceramics," *Materials Today Communications,* vol. 33, p. 104997, 2022.

[25] N. Guo, G. Zhu, H. Xu, X. Jiang, X. Zhang, J. Song, Y. Zhao, K. Jiang, Y. Zhang, Q. Wang, S. Long, T. Wei, and A. Yu, "Preparation of CaF_2 transparent ceramics by cold sintering," *Ceramics International,* vol. 48, no. 23, Part A, pp. 34184–34189, 2022.

[26] B. Liu, K. Sha, Q. W. Zhou, K. X. Song, F. Shi, and Y. H. Cheng, "One-step cold sintering process towards translucent BaF_2 ceramics," *Journal of the European Ceramic Society,* vol. 43, no. 15, pp. 7053–7058, 2023.

[27] J. Hao, J. Guo, C. Ma, F.-Z. Yao, B. Y. M. Si, E. Zhao, and H. Wang, "Cold Sintering of Na_2WO_4 Ceramics using a Na_2WO_4-$2H_2O$ Chemistry," *Journal of the European Ceramic Society,* vol. 41, no. 12, pp. 6029–6034, 2021.

[28] T. Sada, K. Tsuji, A. Ndayishimiye, Z. Fan, Y. Fujioka, and C. A. Randall, "High permittivity $BaTiO_3$ and $BaTiO_3$-polymer nanocomposites enabled by cold sintering with a new transient chemistry: $Ba(OH)_2{\cdot}8H_2O$," *Journal of the European Ceramic Society,* vol. 41, no. 1, pp. 409–417, 2021.

[29] T. Sada, A. Ndayishimiye, Z. Fan, Y. Fujioka, and C. A. Randall, "Surface modification of $BaTiO_3$ with catechol surfactant and

effects on cold sintering," *Journal of Applied Physics,* vol. 129, no. 18, p. 184102, 2021.

[30] P. Pulphol, A. Teandam, T. Charoonsuk, W. Vittayakorn, T. Maluangnont, and N. Vittayakorn, "Fabrication of $BA_5NB_4O_{15}$ ceramics by flux-assisted ultra-low sintering temperature technique," *Suranaree Journal of Science and Technology,* vol. 32, p. 030290, 2025.

[31] S. Zhang, B. Fang, S. Zhang, X. Lu, and J. Ding, "Composition designing and sintering behavior tailoring in $[(Ba_{1-x}Ca_x)_{0.995}Eu_{0.005}](Ti_{1-y}Hf_y)O_3$ multifunctional piezoceramics," *Journal of Alloys and Compounds,* vol. 888, p. 160891, 2021.

[32] K. Wang, Y. Li, J. Li, and G. Zhang, "Boosting interfacial charge separation of $Ba_5Nb_4O_{15}$/g-C_3N_4 photocatalysts by 2D/2D nanojunction towards efficient visible-light driven H_2 generation," *Applied Catalysis B: Environmental,* vol. 263, p. 117730, 2020.

[33] H. Zhao, S. Feng, W. Xu, Y. Shi, Y. Mao, and X. Zhu, "A rapid chemical route to niobates: Hydrothermal synthesis and transport properties of ultrafine $Ba_5Nb_4O_{15}$," *Journal of Materials Chemistry,* vol. 10, no. 4, pp. 965–968, 2000.

[34] H. Guo, A. Baker, J. Guo, and C. A. Randall, "Cold sintering process: A novel technique for low-temperature ceramic processing of ferroelectrics," *Journal of the American Ceramic Society,* vol. 99, no. 11, pp. 3489–3507, 2016.

[35] T. Sada, K. Tsuji, A. Ndayishimiye, Z. Fan, Y. Fujioka, and C. A. Randall, "Highly reliable $BaTiO_3$-polyphenylene oxide nano-composite dielectrics via cold sintering," *Advanced Materials Interfaces,* vol. 8, no. 18, p. 2100963, 2021.

[36] P. Pasierb, S. Komornicki, M. Rokita, and M. Rękas, "Structural properties of Li_2CO_3–$BaCO_3$ system derived from IR and Raman spectroscopy," *Journal of Molecular Structure,* vol. 596, no. 1, pp. 151–156, 2001.

[37] C.-L. Huang, P.-E. Chiang, and T.-H. Hsu, "Influence of intrinsic and extrinsic factors on microwave dielectric properties of $(Sr_{1-x}Mg_x)V_2O_6$ (x = 0.01–0.09) ceramics for ULTCC applications," *Materials Science and Engineering: B,* vol. 273, p. 115438, 2021.

[38] A. Ali, S. Uddin, M. Lal, A. Zaman, Z. Iqbal, and K. Althubeiti, "Structural, optical and microwave dielectric properties of $Ba(Ti_{1-x}Sn_x)_4O_9$, $0 \leq x \leq 0.7$ ceramics," *Scientific Reports,* vol. 11, no. 1, p. 17889, 2021.

[39] K. Du, C. Yin, W. Zhu, C. Zhou, B. Zhang, T. Wang, S. Wang, and W. Lei, "Phase compositions and crystal structure of Sn-deficient $Ca_2Sn_2Al_2O_9$ microwave dielectric ceramics with high Q×f values," *Ceramics International,* vol. 49, no. 1, pp. 202–209, 2023.

[40] J. Iqbal, H. Liu, H. Hao, A. Ullah, M. Cao, and Z. Yao, "Phase, microstructure, and microwave dielectric properties of a new ceramic system: $(1-x)Mg(Ti_{0.95}Sn_{0.05})O_3$–$xCaTiO_3$," *Ceramics International,* vol. 43, no. 16, pp. 14156–14160, 2017.

[41] R. B. Fahim, M. I. Zaki, and G. A. M. Hussien, "Effect of processing parameters on the kinetics of decomposition of certain simple anhydrous carbonates," *Powder Technology,* vol. 33, no. 2, pp. 161–165, 1982.

[42] I. Arvanitidis, D. Siche, and S. Seetharaman, "A study of the thermal decomposition of $BaCO_3$," *Metallurgical and Materials Transactions B,* vol. 27, no. 3, pp. 409–416, 1996.

[43] E. Mgbemeje, M. S. Akhtar, B. Yo, and K. Cd, "Influence of annealing temperatures on the structural, morphological, crystalline and optical properties of $BaTiO_3$ and $SrTiO_3$ nano-particles," *Journal of Material Science & Engineering,* vol. 5, no. 5, p. 1000277, 2016.

[44] C.-Y. Tsao, W.-H. Tuan, and K.-C. Feng, "De-sintering of $Ba_5Nb_4O_{15}$ ceramic and its influence on microwave characteristics," *Journal of the European Ceramic Society,* vol. 37, no. 4, pp. 1517–1521, 2017.

[45] X. Kuang, G. Carotenuto, and L. Nicolais, "A review of ceramic sintering and suggestions on reducing sintering temperatures," *Advanced Performance Materials,* vol. 4, no. 3, pp. 257–274, 1997.

[46] D.-W. Kim, J.-R. Kim, S.-H. Yoon, K. S. Hong, and C. K. Kim, "Microwave dielectric properties of low-fired $Ba_5Nb_4O_{15}$," *Journal of the American Ceramic Society,* vol. 85, no. 11, pp. 2759–2762, 2002.

[47] D.-W. Kim, K. Sun Hong, C. S. Yoon, and C. Kyung Kim, "Low-temperature sintering and microwave dielectric properties of $Ba_5Nb_4O_{15}$–$BaNb_2O_6$ mixtures for LTCC applications," *Journal of the European Ceramic Society,* vol. 23, no. 14, pp. 2597–2601, 2003.

[48] M. Zhang, L. Xin, L. Ren, J. He, L. Ma, and J. Zhai, "Effect of grain morphology and ion diffusion on the dielectric properties of ferroelectric-dielectric composite ceramics," *Materials Technology,* vol. 37, no. 14, pp. 2970–2975, 2022.

[49] C.-L. Huang and K.-H. Chiang, "Structures and dielectric properties of a new dielectric material system $xMgTiO_3$–$(1-x)MgTa_2O_6$ at microwave frequency," *Journal of Alloys and Compounds,* vol. 431, no. 1, pp. 326–330, 2007.